ORIGINAL RESEARCH ARTICLE

Evidence of Magnetocaloric Effect in $(Fe_{63}Ni_{37})_{89}B_{11}$ Nanostructured Magnetic Alloys

D. GARZÓN, C. OSTOS, L.C. SÁNCHEZ, J.M. MARÍN RAMÍREZ, and O. ARNACHE

The magnetocaloric effect associated with magnetic entropy changes (ΔS_M) and phase transitions in $(Fe_{63}Ni_{37})_{89}B_{11}$ (FeNiB) powder alloys was investigated. For this purpose, the particle size of the samples was reduced under milling times of 0 (FNB) and 36 hours (FNB36). X-ray diffraction and Mössbauer spectroscopy results showed the formation of nanostructured magnetic alloys and the coexistence of γ-FCC, α-BCC, and oP-(Fe, Ni)B phases in agreement with the INVAR region. M(H) measurements revealed that both alloys are ferromagnetic soft at room temperature, with coercive field values below ~ 48 Oe. A detailed analysis of the magnetic phase transition using the modified Arrott plot and critical isotherm plots yields critical exponents ($\beta = 0.27$, $\gamma = 0.92$, and $\alpha = 4.4$) close to the theoretical exponents obtained from the Tricritical Mean Field model. Moreover, a maximum magnetic entropy change (ΔS_M) was evidenced around the phase transition (T_C) at ~ 330 K ($-\Delta S_M$ of 2.58 J kg^{-1} K^{-1}) for FNB and ~ 415 K ($-\Delta S_M$ of 0.4 J kg^{-1} K^{-1}) for FNB36 with an applied field of 1.3 T. The relative cooling power and the temperature-averaged entropy change values were determined, and they exhibited a linear dependency as function of the external field. These findings give a good insight towards the advancements of FNB-based alloys for potential room-temperature magnetic refrigeration technology.

https://doi.org/10.1007/s11661-024-07635-x

I. INTRODUCTION

THE current development in materials science is mainly based on the pursuit of the fabrication of functional materials that can be used in various industrial and research applications.[1–3] Furthermore, the production of materials that have a direct impact on the development of greener and sustainable technologies, i.e., those that have a low environmental impact, has recently attracted much attention. In particular, by developing and facilitating technologies that enable an energy transition towards cleaner and more efficient energy sources as an effort to reduce the problems associated with the greenhouse effect and the impact of global warming, in accordance with the Paris Agreement.[4,5]

Within this approach, magnetic refrigeration (MR) can be considered as an optimal option to produce and generate the necessary cooling power that can help overcome the limitations and environmental impacts imposed by the current refrigeration industry. Magnetic cooling technologies do not use greenhouse gases and can therefore be considered environmentally friendly. It is also an energy efficient with a low noise and vibration technology.[4,6–8] MR is based on the magnetocaloric effect (MCE), which is a phenomenon that occurs when an external magnetic field induces a shift in the thermodynamic state of a magnetic material, specifically by changing its adiabatic magnetic entropy (ΔS_M) near the Curie temperature (T_C). Combined with ΔS_M, the relative cooling power (RCP) can quantify the capability of a magnetocaloric material to induce magnetic refrigeration, defined by $RCP = -\Delta S_M{}^{max} \times \delta T_{FWHM}$, where $\Delta S_M{}^{max}$ is the maximum value of the magnetic entropy change, and δT_{FWHM} is the full width at half maximum of the ΔS_M curve. Another important parameter to further evaluate the viability of the compound in MR applications is the temperature-averaged magnetic entropy change (TEC), which can be calculated over a range of temperatures for a given ΔH.[9] Therefore, RCP and TEC parameters are of critical importance when

D. GARZÓN is with the Instituto Tecnológico Metropolitano de Medellín ITM, Calle 73 No 76A-354 Vía al Volador, Medellín, Colombia and also with the Grupo de Estado Sólido-GES, Facultad de Ciencias Exactas y Naturales, Universidad de Antioquia UdeA, Calle 70 No. 52-21, Medellín, Colombia. Contact e-mail: dgarzonv68@gmail.com C. OSTOS, J.M. MARÍN RAMÍREZ and O. ARNACHE are with the Grupo de Estado Sólido-GES, Facultad de Ciencias Exactas y Naturales, Universidad de Antioquia UdeA. L.C. SÁNCHEZ is with the Grupo GAMASCO, Departamento de Física, Universidad de Córdoba, Montería, Colombia.
Manuscript submitted March 5, 2024; accepted October 23, 2024.
Article published online February 5, 2025

discussing the use of MCE in technological applications.[4,6,8–11]

MCE is an intrinsic property of certain magnetic materials, which has led to extensive research on rare earth metals, their alloys, and related compounds due to their significant entropy change and high refrigeration capacity (RCP).[6,12–15] However, these materials are often expensive, limited in availability, and have significant environmental impacts associated with their production.[16–20] As a result, there is growing interest in rare earth-free transition metals, particularly FeNi-based alloys such as FeNiZrB, FeNiMn, FeNiMo, FeNiCr, and FNB, as viable alternatives for magnetocaloric refrigeration (MR) applications. These alloys are more accessible and exhibit significant magnetocaloric response.[21–25] In particular, the γ-FeNi phase at room temperature exhibits a high saturation magnetization (M_s), a low coercive field (H_C), and a Curie temperature (T_C) close to room temperature. Additionally, these materials have high magnetic entropy, which contributes to effective magnetic cooling over a wider temperature range. Boron doping (up to 10 at. pct) allows the Curie temperature to be tuned without affecting their intrinsic magnetic properties. Moreover, the addition of boron reduces the coercive field increasing the saturation magnetization, resulting in improved MCE compared to pure Fe–Ni alloys.[22,23,26]

Additionally, Fe–Ni-based alloys exhibit the so-called INVAR region (65 to 70 at. pct Fe). This INVAR composition refers to the coexistence of two crystalline phases in a small region of the phase diagram. Thus, in Fe-rich alloys, only the body-centered cubic (BCC) or α phase is present, and in Ni-rich alloys, only face-centered cubic (FCC) or γ phase is present. The compositional boundaries of these two phase regions are strongly dependent on the alloy preparation method. This structural competition leads to an anomalous magnetic behavior, where the magnetocaloric response can be enhanced by increasing the presence of the FCC phase.[27,28]

In this work, we have prepared $(Fe_{63}Ni_{37})_{89}B_{11}$—FNB magnetic alloys in the INVAR region by a casting process followed by mechanical alloying. The evidence of magnetocaloric properties were investigated near room temperature seeking the ΔS_M, RCP, and TEC characteristics, and their relationship with their structural and magnetic properties. In addition, critical exponents were obtained near the Curie temperature of the system to predict the magnetic critical behavior and its relationship with the MCE. Hence, the investigation of FeNiB alloys is motivated by their potential to provide sustainable, efficient, and cost-effective solutions for the future of refrigeration technology. By exploring these materials, we can contribute to the development of greener alternatives that are in line with global efforts to combat climate change and promote energy efficiency.

II. EXPERIMENTAL PROCEDURE

Nanoparticles of $(Fe_{63}Ni_{37})_{89}B_{11}$, hereinafter labeled as FNB alloys, were prepared using two experimental techniques widely known as casting and mechanical milling. Details of the alloy synthesis have been reported previously.[21,29] Briefly, a cylindrical FNB pellet with a diameter of 10 mm and a thickness of 3 mm was produced by casting. Next, powder samples of the same material were obtained from bulk FNB alloys using a diamond file. The powdered alloys were grinded under Ar gas in a planetary mill (250 rpm and 20:1 ball-to-power ratio) for different grinding times (0 and 36 hours) at room temperature.

After each 1-hour grinding cycle, a 0.5-hour rest cycle was performed to avoid overheating of the vials with continuous monitoring of the inert atmosphere. Then, the FeNiB powder alloys for two different milling times (Mt), designated as FNB and FNB36, were characterized. For all the FNB samples, the analysis of the phase composition and their crystalline structure was performed by X-ray diffraction (XRD) technique, using a PANalytical Empyrean series 2 (CuKα 1.5405 Å). The Rietveld refinement was performed using the FullProf software. The analysis of the chemical environment was performed by Mössbauer spectroscopy (MS) technique using a conventional spectrometer with a ^{57}Co(Rh) radioactive source at room temperature in transmission geometry. All spectra were fitted using the standard α-Fe absorber as a calibration, and their hyperfine parameters were obtained using the Recoil program.[30] The microstructural analysis was also performed by electron microscopy techniques using both a scanning electron microscope (SEM-EDX) with a JEOL-JSM 6490LV microscope, and a high-resolution transmission electron microscope (HRTEM) with an FEI Tecnai F20 Super Twin TMP. The elemental composition was completed using a Thermo Fisher wavelength dispersive X-ray fluorescence spectrometer (WDXRF). Finally, the magnetic characterization was performed using a vibrating sample magnetometer (VSM) module attached to a PPMS—Quantum Design system.

III. RESULTS AND DISCUSSION

A. *Microstructural Analysis*

XRD patterns of the FNB and FNB36 powder alloys are shown in Figure 1. Rietveld refinement of these patterns revealed the coexistence of three crystalline phases corresponding to a face-centered cubic (γ-FCC) structure ($Fm\bar{3}m$), a body-centered cubic (α-BCC) structure ($Im\bar{3}m$), and a primitive orthorhombic (oP) structure (Pnma). The conventional reliability R-factors of the Rietveld refinement with all non-excluded points and lattice parameters for both alloys are shown in Table I. For the case of FNB [Figure 1(a)], the alloy crystallizes in a highly (111)-oriented 63 pct γ-FCC Ni-rich Fe phase, commonly known as taenite.[24,31] This phase is typical of iron–nickel systems ($Fe_{50}Ni_{50}$) and iron–nickel-based parent alloys such as $(Fe_{70}Ni_{30})_{100-x}B_x$[24,32,33]; a 5 pct α-BCC Fe-rich Ni phase and a 32 pct oP (Fe,Ni)B phase were also found. After 36 hours of mechanical milling [Figure 1(b)], the FNB36 alloy showed the formation of randomly

oriented nanocrystallites with a 41 pct γ-FCC phase, a 30 pct α-BCC phase, and a 29 pct oP (Fe,Ni)B phase conformation, with lower intensity values and broader diffraction peaks than those observed for FNB. It is noticeable that the α-BCC phase increased in a similar at. pct range as the γ-FCC phase decreased, while the oP (Fe, Ni)B phase remained almost constant. These results are in good agreement with those reported in the INVAR region of the $(Fe_{63}Ni_{37})_{89}B_{11}$ parent alloy.[28] In addition, the main γ-FCC and α-BCC reflection peaks shifted towards lower 2θ angles, resulting in larger cell volumes, suggesting an increase in iron content in the FNB36 cubic crystalline phases. An opposite behavior was observed for the oP phase due to a decrease in cell volume as a result of iron–nickel segregation. These observations could be associated with a continuous decrease in the crystallite size and its deformation at the atomic level by the introduction of lattice strain[34–36]; explained by local atomic differences in the crystallites and the diffusion effects during the milling process.

The average grain size and crystalline structure of the FNB36 alloy were examined using HRTEM. The analysis included estimates of nanoparticle sizes [Figure 2(a)], high-resolution images, and selected area electron diffraction (SAED) patterns for interplanar spacing [Figure 2(b)], and a histogram of nanoparticle distributions with a log-normal curve for mean particle size estimation [Figure 2(c)]. After 36 hours of milling, the average particle size was approximately 5.8 nm, with an interplanar distance of about 20.7 nm.

B. *Magnetic Properties*

Figure 3 shows the Mössbauer spectra at room temperature with the corresponding fitting model. The fitting model for both systems consists of five crystallographic sites (one singlet and four sextets). The determined hyperfine parameters obtained from the fits are listed in Table II. The results confirm the coexistence of γ-FCC Fe–Ni alloys, which decompose into two γ-FCC phases. The first one is Ni-rich and ferromagnetic giving rise to a Mössbauer Sextet-1, and the other is non-magnetic Fe-rich, resulting in a Mössbauer singlet. The other magnetic sites are related to the α-BCC (Sextet-2) and oP-(Fe,Ni)B (Sextet-3 and Sextet-4) structural phases, in agreement with the XRD analysis.[33,34] The FNB and FNB36 singlets with $\delta = -0.04$ and -0.05 mm/s corresponding to the paramagnetic phase characteristic of the low-spin (antitaenite) γ-FCC, and Sextet-1 with hyperfine fields $B_{hf} = 31.7$ and 30.4 T resulting from and the high-spin (taenite) γ-FCC phase, are in agreement with those observed in the previous studies on samples prepared by different techniques for FeNi INVAR alloys.[28,37] The Sextet-2 with hyperfine fields $B_{hf} = 32.3$ and 33.1 T for FNB and FNB36, respectively, are associated with α-FeNi and Sextex-3 and Sextet-4 with $B_{hf} = 24.7$ and 21.9 T for FNB and $B_{hf} = 23.3$ and 20.2 T for FNB36, respectively, are in agreement with those reported by other authors[38,39] for the FNB alloys, corresponding to a local environment similar to that of the orthorhombic $(FeNi)_3B$. In addition, it is worth noting that the relative areas of the γ-FCC, α-BCC, and oP-(Fe,Ni)B contributions obtained by MS are in very good agreement with those obtained by XRD. In general, it can be inferred that mechanical milling at a higher time leads to an increase in the α-BCC phase at the expense of the high-spin (taenite) γ-FCC phase, which is associated with a decrease in particle size. It should be noted that it is not possible to resolve the low-spin FCC phase from the high-spin FCC phase by using the XRD technique.

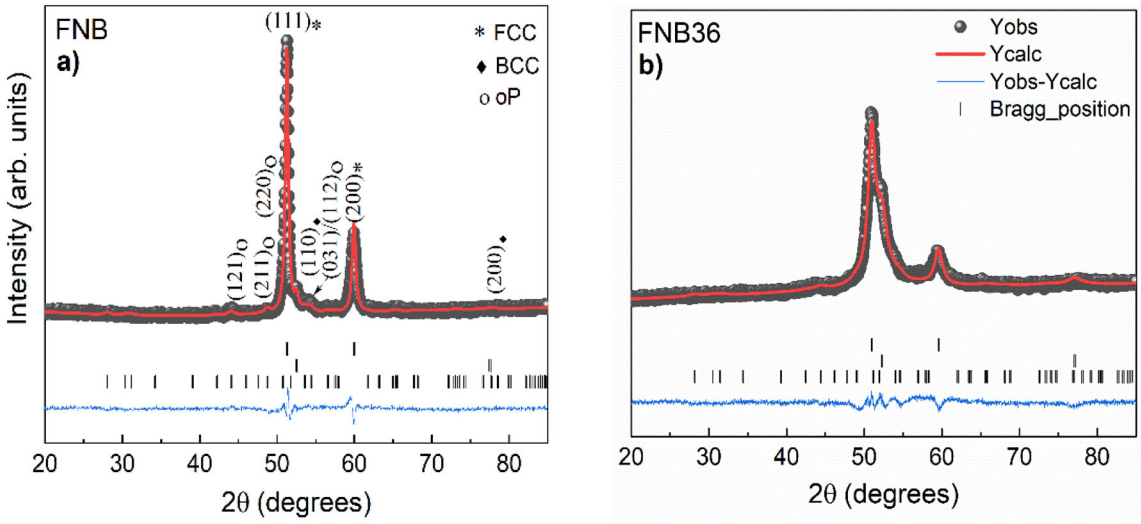

Fig. 1—XRD patterns for the FNB and FNB36 alloys. Black dots are the experimental data while the continuous red line corresponds to the Rietveld fit. Bragg positions are indicated by vertical bars (top-down: γ-FCC, α- BCC, and oP) and the difference is the bottom blue line (Color figure online).

Table I. Lattice Parameters and Conventional Reliability R-factors (Rp, Rwp, Re, c^2) of the Rietveld Refinement with all Non-excluded Points (Primitive Orthorhombic-oP, Face-Centered Cubic γ-FCC, Body-Centered Cubic α-BCC)

Alloy	Crystalline Phase	At. pct	Lattice Parameters (Å)	Volume (Å)^3	R-factors (Rp, Rwp, Re, c^2)
FNB	γ-FCC	63	a = 3.5833(5)	46.01(1)	24.3, 16.7, 10.4, 2.61
	α-BCC	5	a = 2.8601(8)	23.40(1)	
	oP	32	a = 5.356(2)	158.4(1)	
			b = 6.662(4)		
			c = 4.439(1)		
FNB36	γ-FCC	41	a = 3.604(2)	46.81(4)	18.2, 14.0, 8.79, 2.56
	α-BCC	30	a = 2.873(1)	23.71(2)	
	oP	29	a = 5.329(5)	155.8(3)	
			b = 6.608(9)		
			c = 4.423(3)		

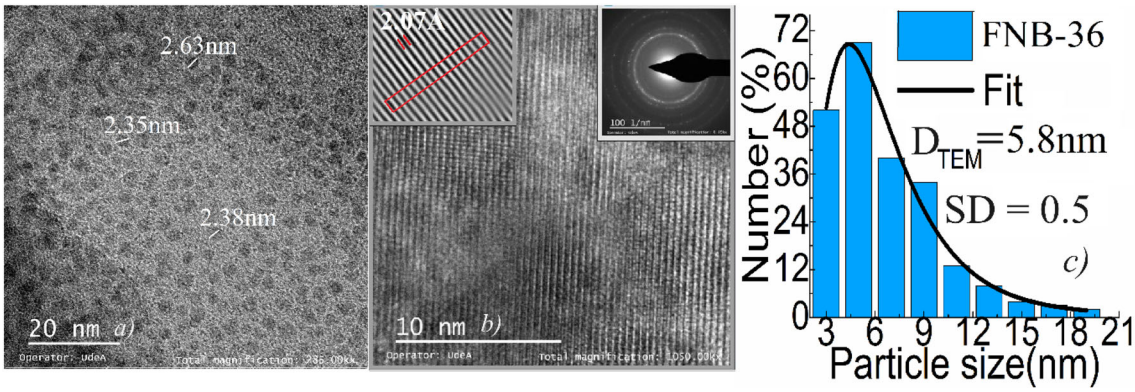

Fig. 2—Bright-field TEM images for the FNB36 powder alloys. (*a*) Nanoparticles dispersed in the copper matrix in which they were deposited for the analysis, (*b*) high-resolution field image with SAED and fringe patterns to determine interplanar distances (insets).

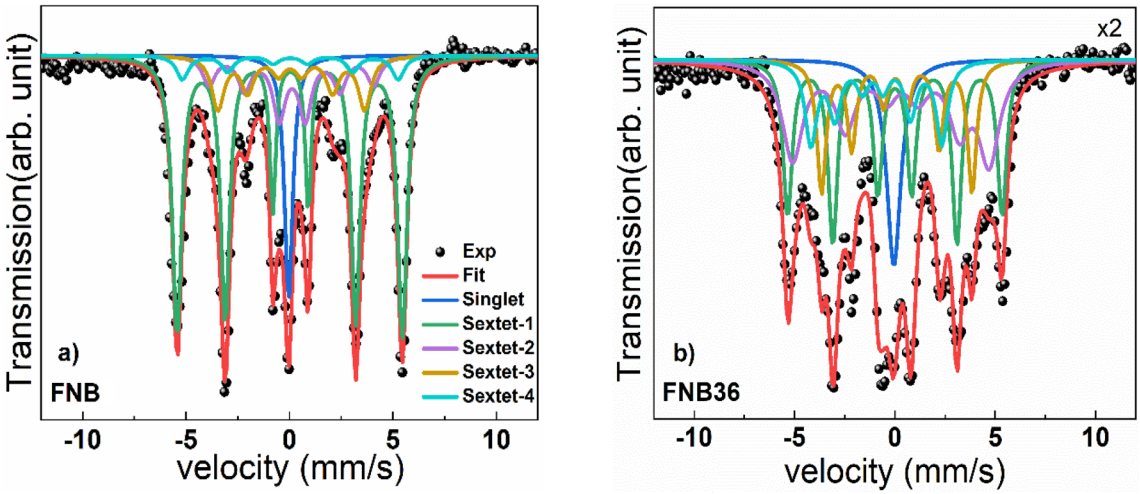

Fig. 3—Room temperature Mössbauer spectra and corresponding fitting sites for the (*a*) FNB and (*b*) FNB36 powder alloys.

Figure 4 shows the temperature dependence of the magnetization M(T) for the FNB alloy under a field of 100 Oe. The Curie temperature was determined using a minima dM/dT vs T plot (inset of Figure 4),[40] obtaining a value of T_C ~ 330 K for FNB and a T_C ~ 415 K for the FNB36 sample. These T_C values for FNB and FNB36 nanoparticles are lower than those reported in the FeNi phase diagram presented by the authors in Reference 41. Such a change can be attributed to atomic rearrangements (short-range ordering or clustering by

Table II. Mössbauer Hyperfine Parameters for the FeNiB Alloys Before (0 h) and After Milling (36 h)

Component	B_{hf} (T)	δ (mm/s)	2ε (mm/s)	RA (pct)
FNB				
Singlet	—	− 0.04 (1)	—	9 (1)
Sextet-1	31.7 (2)	0.03 (1)	− 0.04 (1)	54 (2)
Sextet-2	32.3 (2)	0.04 (1)	0.00 (1)	6 (1)
Sextet-3	24.7 (1)	0.11 (2)	− 0.04 (1)	17 (1)
Sextet-4	21.9 (2)	0.06 (1)	0.06 (2)	14 (1)
FNB36				
Singlet	—	− 0.05 (1)	—	10 (1)
Sextet-1	30.4 (1)	0.09 (2)	− 0.08 (1)	29 (1)
Sextet-2	33.1 (3)	0.01 (1)	0.00 (1)	33 (2)
Sextet-3	23.3 (2)	0.06 (1)	0.08 (2)	16 (1)
Sextet-4	20.8 (2)	0.11 (1)	0.18 (2)	12 (1)

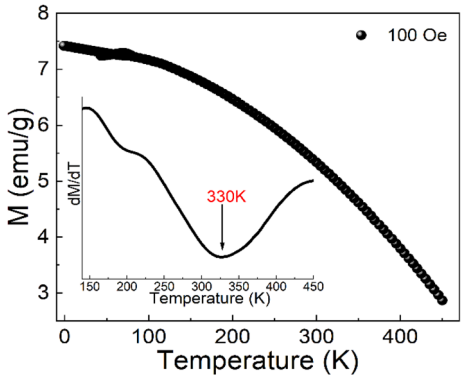

Fig. 4—Magnetization as a function of the temperature for the FNB alloy using field-cooled (FC) conditions with an external applied field of 100 Oe. Inset shows the corresponding Curie temperature T_C extracted from the dM/dT *vs* T plot.

boron addition) and low-energy milling.[29,42,43] Figure 5(a) (inset) highlights the magnetization versus field M(H) isotherms taken at 300 K for the FNB (blue) and FNB36 (black) alloys. The obtained values for the coercive field (H_C) and saturation magnetization (M_S) were ~ 22.9 and ~ 47.2 Oe and ~ 112 and ~ 142 emu/g, respectively. Therefore, as expected, both samples are soft magnetic and exhibit high M_S values, compared to similar alloys produced by mechanical milling, melt spinning, furnace melting, among others.[22,27,44,45]

To further understand the nature of magnetic phase transitions and the critical behavior under scaling assumptions,[22,32] 36 M(H) isotherms were measured for both alloys. For the FNB alloy system, the measurements were taken from 290 K to 360 K, with a ΔT = 2 K. For the FNB36 alloys, the curves were measured from 374 K to 450 K with a ΔT = 2 K. Thus, for both systems, it was ensured that the measurements were taken in the proximity of T_C. Figure 5(a) and (c) shows the M(H) isotherms for both systems, while Figure 5(b) and (d) displays the temperature variation (ΔT) at which all isotherms were recorded.

C. *Critical Exponents (c-exp) and Magnetic Behavior in FNB Alloys*

The critical behavior is commonly investigated using a series of critical exponents (β, γ, δ, η) in the vicinity of the Curie temperature T_C,[22,32,46] where β refers to the behavior of the magnetization M(T) with respect to temperature, γ to the inverse of the magnetic susceptibility (χ^{-1}), δ to the critical isotherm at T_C, and η to the field-dependent magnetic entropy change. Therefore, this c-exp will lead to a better understanding of the magnetocaloric behavior of the FNB and FNB36 alloys. Equations [1] to [3] show the c-exp relationship with the magnetic properties for any magnetic system.

$$M_s(T) = M_0(-\varepsilon)^{\beta}, \varepsilon > 0, T < T_C \quad [1]$$

$$\chi_0^{-1}(T) = \left(\frac{h_0}{M_0}\right)\varepsilon^{\gamma}, \varepsilon > 0, T > T_C \quad [2]$$

$$M = DH^{\frac{1}{\delta}}, \varepsilon = 0, T = T_C, \quad [3]$$

where $\varepsilon = (T - T_C)/T_C$ is the reduced temperature, h_0/M_0 and D are the critical amplitudes. In the asymptotically critical region ($|\varepsilon| < 0.1$), the critical exponents (β, γ) must obey the Arrott–Noakes equation[24,32,46] described by Eq. [4].

$$\left(\frac{H}{M}\right)^{1/\gamma} = \frac{T - T_C}{T_C} + bM^{1/\beta}, \quad [4]$$

where b is a material-specific constant and γ and β are critical exponents. The exponents γ and β can be determined by fitting the $M_S(T)$ and $\chi_0^{-1}(T)$ curves using the modified Arrott plot of $M^{1/\beta}$ *vs* $(H/M)^{1/\gamma}$. Meanwhile, the exponent δ can be estimated by fitting the $M(H)$ curve at T_C according to Eq. [3].

These exponents are directly related to the MCE of the materials. For example, using the Arrott–Noakes equation of state,[22,24,47,48] the change in magnetic entropy (ΔS_M) T_C can be expressed by Eq. [5]:

$$\Delta S_M = -\frac{\alpha\beta\gamma}{b^{\frac{\beta+\gamma\beta}{\beta+\gamma}}(2\beta+\gamma-1)}H^{\frac{(\beta-1)}{(\beta+\gamma)}+1} = AH^n, \quad [5]$$

where n is a parameter and is related to the critical exponents β and γ at/near the T_C as $n(\beta, \gamma) = 1 + [(\beta - 1)/(\beta + \gamma)]$, a and b are constants, and A is a function of the critical exponents. Similarly, there is a dependence of RCP on the magnetic field (RCP $\propto H^N$), where $N = 1 + 1/\delta$. Therefore, it is useful to determine γ, β, and δ to evaluate the RCP in magnetic materials at any magnetic field. Figures 6(a) and 7(a) show the Arrott plot of $M^{\{\frac{1}{\beta}}vs(H/M)^{\frac{1}{\gamma}}$ for FNB and FNB36. This plot is a helpful tool to identify first-order phase transitions (FOPT) or second-order phase transitions (SOPT). According to Banerjee's criterion,[49,50] the slope of the line in the Arrott plot indicates the order of the phase transition: a negative slope ($m < 0$) corresponds to FOPT, while a positive

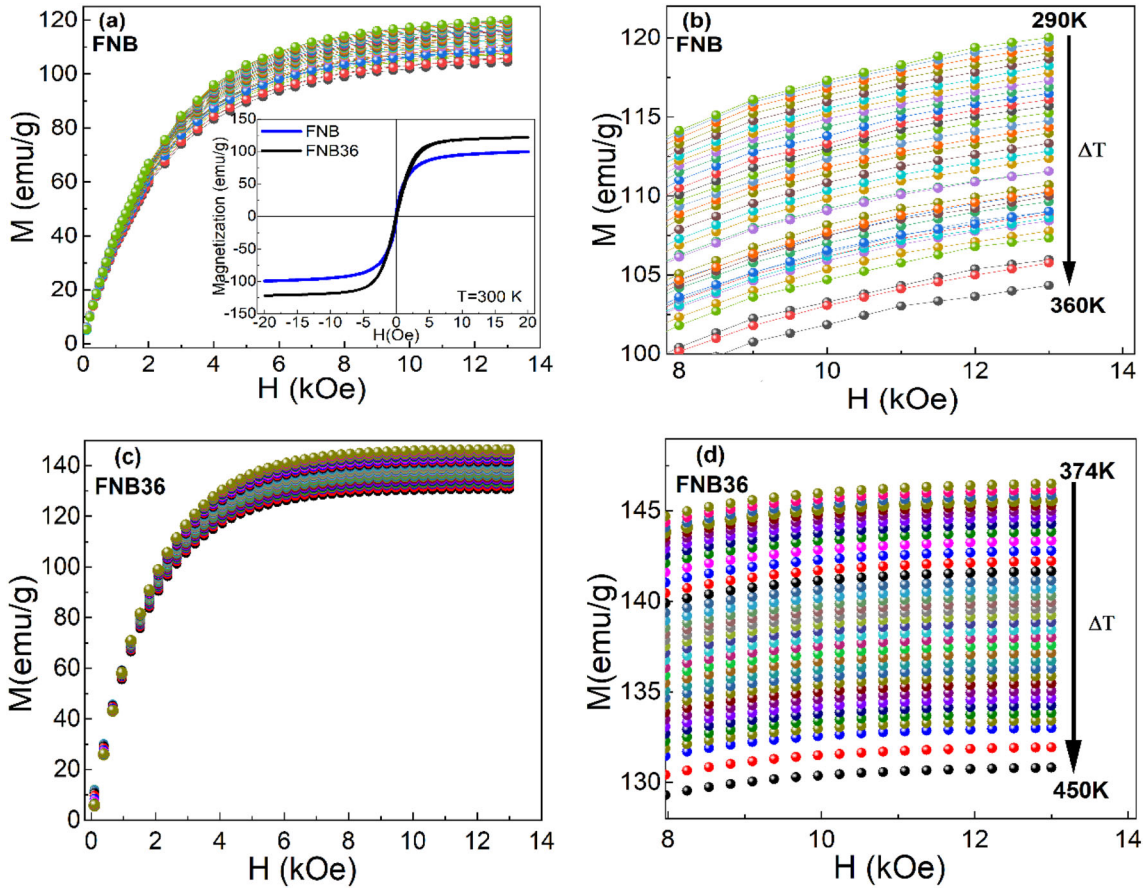

Fig. 5—(*a*) M(*H*) isotherms of FNB from 290 K to 360 K, (*b*) M(H) zoom of FNB alloys for H_{appl} between 9.5 and 14 kOe (circled), (*c*) M(*H*) isotherms of FNB36 nanoparticles from 374 K to 450 K and (*d*) M(*H*) magnification of FNB36 alloys for H_{appl} between 9.5 and 14 kOe. The inset in (*a*) shows M(H) isotherms at 300 K for FNB and FNB36.

slope ($m > 0$) corresponds to SOPT. Therefore, Arrott's Figures 6(a) and 7(a) indicate a SOPT for both alloys, according to the measurement of the curve at T_C. It was observed that all $M^{\frac{1}{\beta}} vs (H/M)^{\frac{1}{\gamma}}$ curves show almost straight lines with positive slopes, even at high magnetic fields (greater than 0.05 kOe), the Arrott curves are not parallel to each other, indicating the absence of long-range mean-field interactions and the Landau mean-field model is not satisfied for $\beta = 0.5$ and $\gamma = 1.0$.[22,51,52] Therefore, modified Arrott plots (MAP) were used to determine the critical behavior and the nature of the transition, as proposed by the Arrott–Noakes Eq. [4].

Figures 6(b–d) and 7(b–d) show the MAP using the theoretical values of the exponents β and γ used.[22,53,54]

From the relative slopes (RS), it was evidenced that both the Ising-3D model and the Heisenberg-3D model were found to be close to 1 below and above T_C [see inset Figures 6(a) and 7(a)]. This result indicates that the critical behavior of FNB and FNB36 may not belong to a single universality.[47,48] However, according to the trend of the relative slopes, it can be said that these systems have a better agreement with the Ising-3D model.[22,55] Using the Widom relation ($\delta = 1 + \gamma/\beta$)[24,54] and Eqs. [1] to [3] at $T = T_C$, we found that c-exp for both systems were $\delta = 4.4$, $\gamma = 0.92$, $\beta = 0.27$ in FNB and $\delta = 4.6$, $\gamma = 0.90$, and $\beta = 0.25$ in FNB36. In addition, the $n(\beta, \gamma)$ values relating ΔS_M to H Eq. [5] were 0.4 and 0.35 in both alloys, respectively.

D. *Magnetocaloric Effect (MCE) in FeNiB Alloys*

To study the MCE in our systems, the magnetic entropy change ($-\Delta S_M$) was calculated from the M(H) isotherms in the vicinity of the T_C, at temperature intervals $\Delta T = 2$ K and fields between 4 and 13 kOe. This change in magnetic entropy ($-\Delta S_M$) was calculated using Maxwell's relation ($\Delta S_M = \int_0^H \left(\frac{\partial M}{\partial T}\right)_H dH$).[22,53]

The ΔS_M *vs* T curves obtained for both alloys for applied magnetic fields of 4 to 13 kO3 are shown in Figure 8(a) and (b). In the FNB alloy the temperature

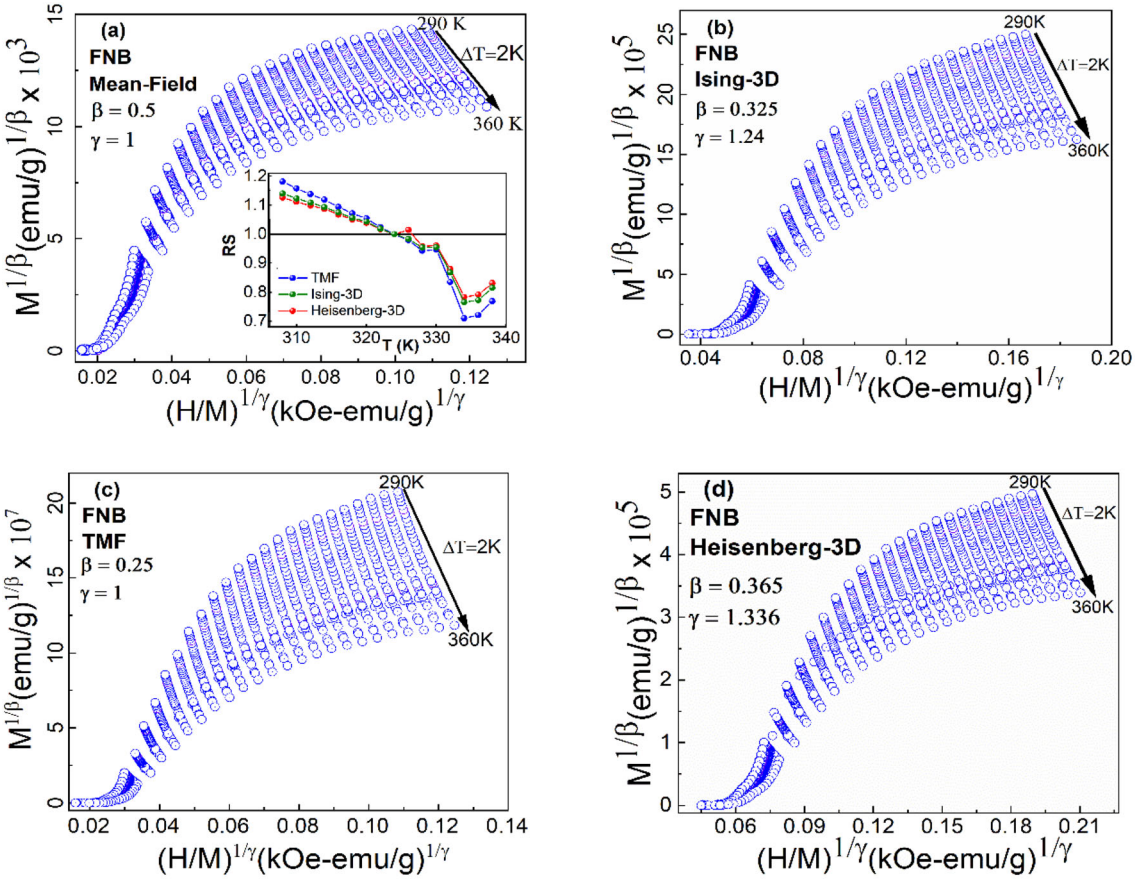

Fig. 6—Critical exponents of FNB. Arrott plot for the (a) Mean field model, (b) 3D-Ising model, (c) Tricritical mean-field (TMF) model, and (d) 3D-Heisenberg model, the inset in (a) shows the relative slopes $RS = S(T)/S(T_C)$ as a function of temperature.

range in which $-\Delta S_M$ was observed ranges from 328 K to 337 K, with a maximum $-\Delta S_M{}^{\max}$ of 2.58 J kg^{-1} K^{-1}, while in the FNB36 alloy, $-\Delta S_M$ was recorded in a higher temperature range (355 to 384 K) with a maximum value for $-\Delta S_M{}^{\max}$ of 0.4 J kg^{-1} K^{-1}.

From the data of the theoretical models shown in Figures 6 and 7, the calculated values of n were 0.66 for the Arrott plot and *0.68*, *0.57*, and *0.4* for the MAP.[22,32,56] Figures 9(a, b) illustrates the field-dependent behavior of DS_M. The values associated with DS_M were obtained using three different fitting functions: Gaussian (Brown), Lorentzian (Blue), and Manual (Green). Likewise, the corresponding RCP values for each fitting function are shown in Figures 9c, d. Both DS_M and RCP increase proportionally with the applied magnetic field independent of the fitting function. This dependence is elucidated by a power-law analysis, represented by $DS_M = AH^n$, and $RCP = AH^N + b$, where A and b are fitting parameters, while n and N denote the respective power function. The results associated with each fitting function and the corresponding fitting parameters are shown in Table III. The best fitting function to the experimental values was the Gaussian fit with a $R^2 = 0.988$. It is noticeable that the values of N for FNB and FNB36 are almost identical, with an RCP at 13 kOe equal to 10.1 J kg^{-1} and 5.3 J kg^{-1}, respectively. These values show a substantial agreement with the value derived from critical exponents using the TMF model ($N = 1.2$, $\delta = 4.4$, and $\delta = 4.6$).[22,24,55–57]

For a proper interpretation of high RCP materials, L.D. Griffith *et al.*[58,59] suggested using the figure of merit (FOM) related to the temperature-averaged entropy change $\left(\text{TEC} \approx \frac{\left[\Delta S_{iso}\left(T_{pk}-\frac{\delta}{2}\right)+\Delta S_{iso}\left(T_{pk}\right)+\Delta S_{iso}\left(T_{pk}+\frac{\delta}{2}\right)\right]}{3}\right)$, where ΔS_{iso} is isofield magnetization data and T_{pk} is the temperature corresponding to $|\Delta S_M^{\max}|$, which is crucial for assessing the performance of magnetocaloric materials.[9,58,59]

Figure 10 shows the TEC(3) *vs.* H, both alloys exhibit an increasing trend with the applied field as reported by L.D. Griffith et al.[9]. However, in the FNB36 sample, the TEC(3) value at $H = 1$ T decreases by approximately 21.6 pct compared to the FNB sample, indicating

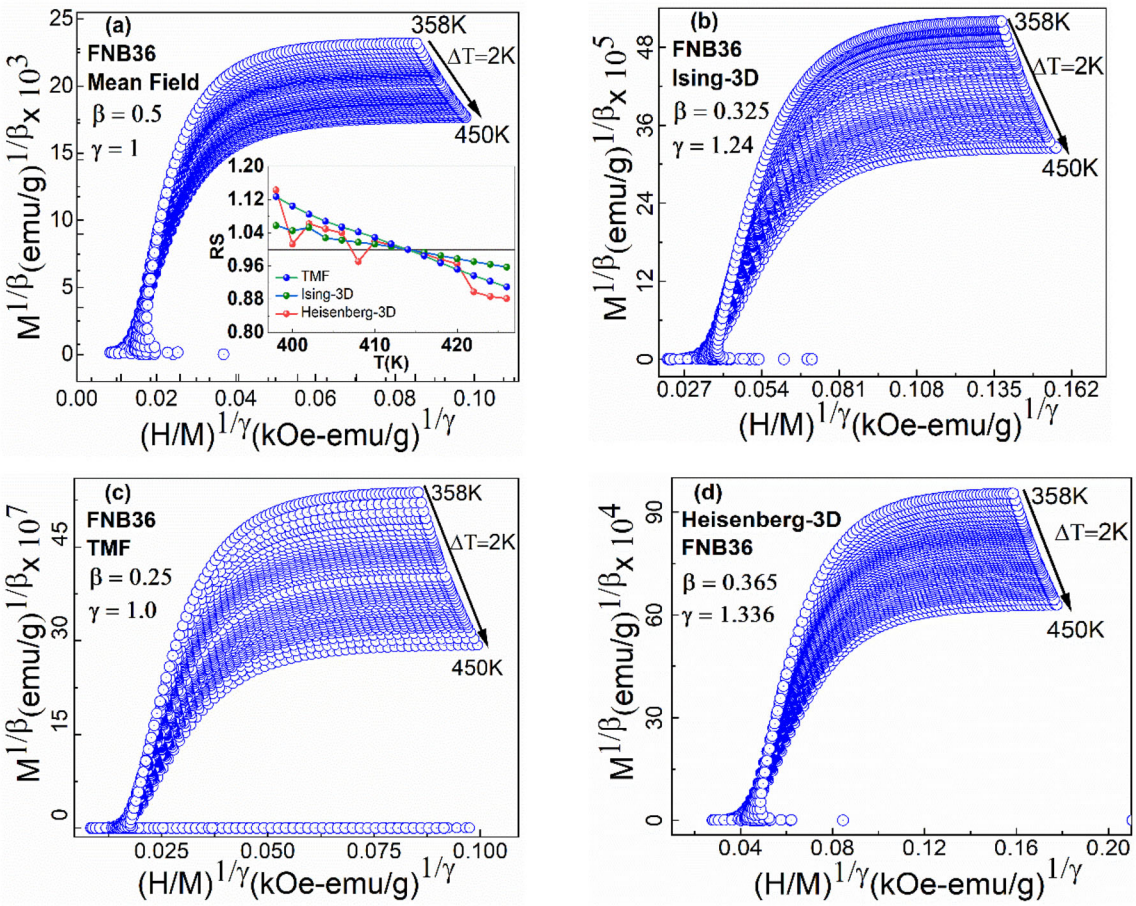

Fig. 7—Critical exponents of FNB36. Arrott plot for the (*a*) Mean field model, (*b*) 3D-Ising model, (*c*) Tricritical mean-field (TMF) model, and (*d*) 3D -Heisenberg model. The inset in (*a*) shows the relative slopes $RS = S(T)/S(T_C)$ as a function of temperature.

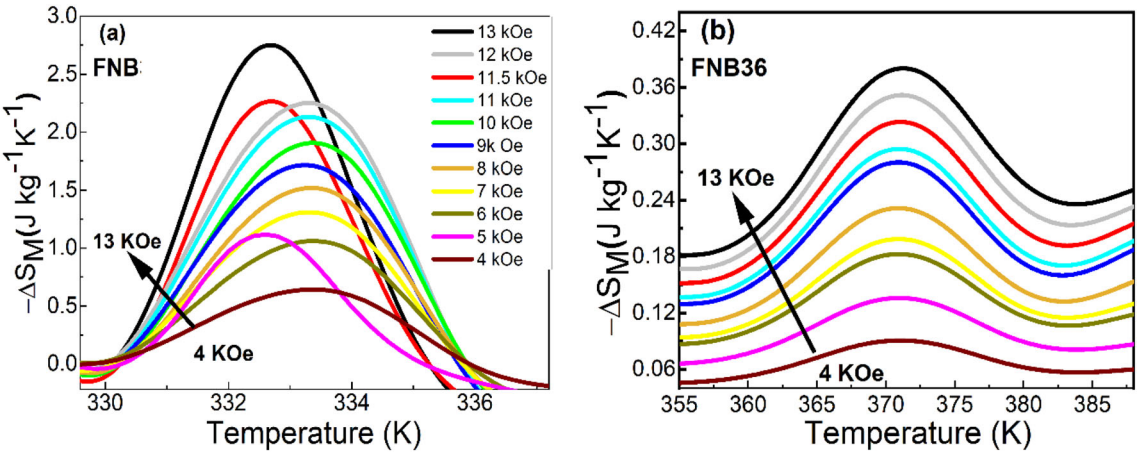

Fig. 8—Magnetic entropy change ($-\Delta S_M$) for both FNB and FNB36 alloys as a function of temperature T, with external field variations from 0.4 to 13 kOe. (*a*) FNB with temperature ranges from 328 to 337 K and (*b*) FNB36 with temperature ranges between 355 and 384 K.

that mechanical milling reduces the TEC in the FeNiB alloys. Furthermore, the TEC(3) (1.7, 0.4) J $Kg^{-1}K^{-1}$ values for $H = 1.3$ T in both alloys are comparable to those reported for the manganite $LaKMnO_3$, Tb-SMM, and Dy-SMM systems.[9,60]

Finally, in the context of the magnetic phase transition from ferromagnetic to paramagnetic, the values of

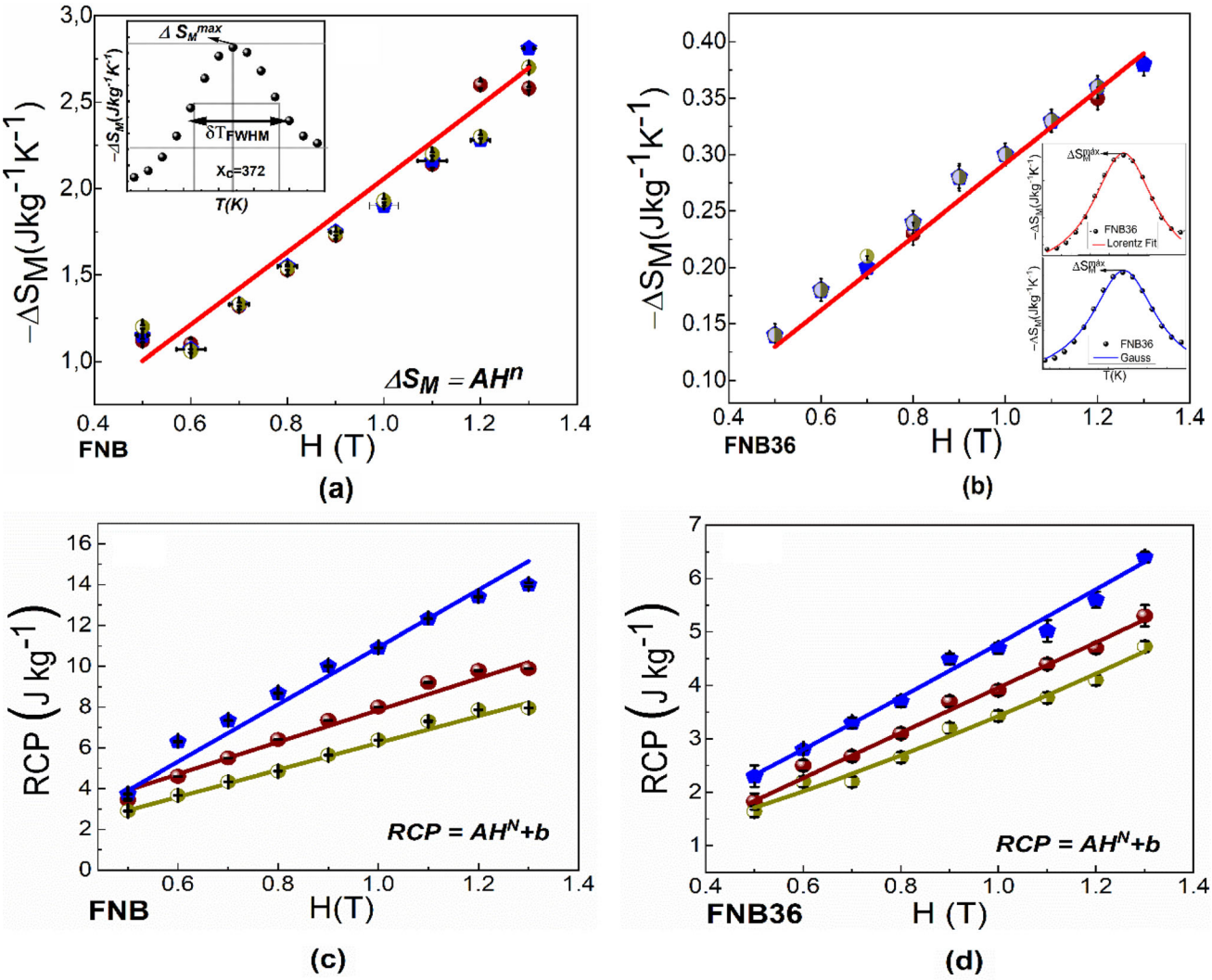

Fig. 9—(*a*), (*b*) $-\Delta S_M^{max}$ as a function of applied field (ΔH) for the range *0.4 T* and *1.3 T*, experimental data are described by dots and the solid lines are the power-law fit ($\Delta S_M = AH^n$), (*c*), (*d*) three fitting methods (Brown—Gaussian, Blue—Lorentzian, Green—Manual) for RCP data using $RCP \propto H^N$ fit.

n = 1.03 for FNB and n = 1.0 for FNB36, which closely match with the n value (0.925) obtained in comparable multiphase FNB alloys.[24] These results suggest that $n > 1$ is attributed to the partial contribution of α-Fe-Ni-B ferromagnetic interactions.[22,24,56]

IV. CONCLUSIONS

The microstructural, magnetic, and magnetocaloric effects of the $(Fe_{63}Ni_{37})_{89}B_{11}$ (FNB) nanostructured magnetic alloys were obtained and compared with the prepared parent alloy by the casting process. The particle size of the alloys was reduced by mechanical milling for up to 36 hours. XRD patterns and Mössbauer spectra confirmed the formation of nanostructured magnetic alloys with the coexistence of γ-FCC, α-BCC and oP-(Fe,Ni)B phases, where the γ-FCC being partially transformed into α-BCC with increasing milling time as a result of iron segregation from the oP to the cubic phases. Therefore, the behavior of Fe in these alloys plays a significant role by inducing changes in the Curie temperature. According to the values of the critical exponents obtained experimentally for the FNB and FNB36 alloys, both systems can be described by the Tricritical Mean Field (TMF) model. The results for the

Table III. n and N Exponents for $\Delta S_M(H)$ and RCP(H) Obtained by Fitting Functions Gaussian, Lorentzian, and Manual Fitting))

Alloy				
$\Delta S_M(H) = AH^n$				
	n	A		R^2
FNB	1.03 ± 0.08	2.05 ± 0.05		0.955
FNB36	1.00 ± 0.03	0.30 ± 0.01		0.994
$RCP\ (H) = A^*H^N + b$				
	N	A^*	b	R^2
FNB				
Gaussian-Fit	1.22 ± 0.03	7.9 ± 0.6	− 0.03 ± 0.02	0.988
Lorentzian-Fit	1.2 ± 0.0	12.3 ± 0.6	− 1.3 ± 0.4	0.981
Manual-Fit	1.2 ± 0.3	5.3 ± 0.4	0.6 ± 0.2	0.985
FNB36				
Gaussian-Fit	1.23 ± 0.21	4.2 ± 0.6	− 0.2 ± 0.2	0.988
Lorentzian-Fit	1.1 ± 0.3	4.5 ± 0.7	0.2 ± 0.1	0.985
Manual-Fit	1.2 ± 0.4	2.8 ± 0.3	0.5 ± 0.2	0.973

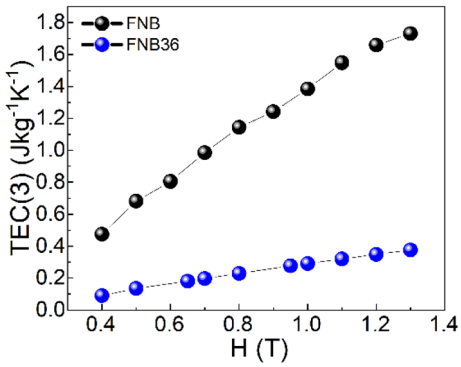

Fig. 10—Magnetic field dependence of the temperature-averaged entropy change at 3 K TEC(3).

$-\Delta S_M$ under an applied field of 1.3 T were 2.6 J kg^{-1} K^{-1} and 0.4 J kg^{-1} K^{-1} for FNB and FNB36 alloys, respectively, and the corresponding RCP values were 10.1 J kg^{-1} and 5.3 J kg^{-1}, respectively. In addition, the TEC(3) values for the FeNiB alloys were 1.7 and 0.4 J Kg^{-1} K^{-1} at H = 1.3 T. These results confirm the evidence of the MCE in the nanostructured magnetic alloys with the maximum range of values around the TC, which are close to room temperature.

ACKNOWLEDGMENTS

Dr. D. Garzón wishes to express his gratitude to MinCiencias, Colombia, for his PhD fellowship under contract 7851-2017 and to Dr. O. Vázquez-Robaina for valuable discussions on specific aspects. The authors thank the financial support by Solid State Group—GES in the framework of Sustainability Strategy 2023, and CODI projects 2017-16368 and 24-1-1529 of the Universidad de Antioquia, Colombia.

FUNDING

Open Access funding provided by Colombia Consortium.

CONFLICT OF INTEREST

On behalf of all authors, the corresponding author states that there is no conflict of interest.

OPEN ACCESS

REFERENCES

1. P. Kumari, A.K. Gupta, R.K. Mishra, M.S. Ahmad, and R.R. Shahi: *J. Magn. Magn. Mater.*, 2022, vol. 554, p. 169142.

2. C. Zhang, X. Li, L. Jiang, D. Tang, Xu. Han, P. Zhao, Fu. Jianzhong, Q. Zhou, and Y. Chen: *Adv. Funct. Mater.*, 2021, vol. 31, p. 2102777.
3. M. Gao, D. Miracle, D. Maurice, X.-H. Yan, Y. Zhang, and J. Hawk: *J. Mater. Res.*, 2018, vol. 33, pp. 3138–3155.
4. V. Franco, J.S. Blazquez, B. Ingale, and A. Conde: *Annu. Rev. Mater. Res.*, 2012, vol. 42, pp. 305–342.
5. L. Mañosa and A. Planes: *J. Phys. D Appl. Phys.*, 2018, vol. 51, 070201.
6. M.-H. Phan and Yu. Seong-Cho: *J. Magn. Magn. Mater.*, 2007, vol. 308, pp. 325–340.
7. Y. Zhang, Xu. Peng, J. Zhu, S. Yan, J. Zhang, and L. Li: *Mater. Today Phys.*, 2023, vol. 32, p. 101031.
8. J.U. Ahamed, R. Saidur, and H.H. Masjuki: *Renew. Sustain. Energy Rev.*, 2011, vol. 15, pp. 1593–1600.
9. L.D. Griffith, Y. Mudryk, J. Slaughter, and V.K. Pecharsky: *J. Appl. Phys.*, 2018, vol. 123, p. 034902.
10. J. Romero Gómez, R. Ferreiro Garcia, A. De Miguel Catoira, and M. Romero Gómez: *Renew. Sustain. Energy Rev.*, 2013, vol. 17, pp. 74–82.
11. N.R. Ram, M. Prakash, U. Naresh, N.S. Kumar, T.S. Sarmash, T. Subbarao, R.J. Kumar, G.R. Kumar, and K.C. Naidu: *J. Supercond. Novel Magn.*, 2018, vol. 31, pp. 1971–1979.
12. Y. Yuan, Y. Wu, X. Tong, H. Zhang, H. Wang, X.J. Liu, L. Ma, H.L. Suo, and Z.P. Lu: *Acta Mater.*, 2017, vol. 125, pp. 481–489. https://doi.org/10.1016/j.actamat.2016.12.021.
13. M. Feuerbacher, M. Heidelmann, and C. Thomas: *Mater. Res. Lett.*, 2015, vol. 3, pp. 1–6. https://doi.org/10.1080/21663831.2014.951493.
14. M.M. Elkenany, S.H. Aly, and S. Yehia: *Cryogenics*, 2022, vol. 123, p. 103439. https://doi.org/10.1016/j.cryogenics.2022.103439.
15. F. Scheibel, W. Liu, L. Pfeuffer, N. Shayanfar, A. Taubel, K.P. Skokov, S. Riegg, Wu. Yuye, and O. Gutfleisch: *J. Appl. Phys.*, 2023, vol. 133, p. 7.
16. J.Y. Law, Á. Díaz-García, L.M. Moreno-Ramírez, and V. Franco: *Acta Mater.*, 2021, vol. 212, p. 116931.
17. M. Ge, Du. Haifeng, C. Jin, W. Wei, J. Fan, C. Zhang, Li. Pi, and Y. Zhang: *Sci. Rep.*, 2016, vol. 6, p. 22397.
18. J. Liu, G. Qu, X. Wang, H. Chen, Y. Zhang, G. Cao, R. Liu, S. Jiang, H. Shen, and J. Sun: *J. Alloys Compd.*, 2020, vol. 845, p. 156190.
19. H. Wilhelm, M. Baenitz, M. Schmidt, U.K. Rößler, A.A. Leonov, and A.N. Bogdanov: *Phys. Rev. Lett.*, 2011, vol. 107, p. 127203.
20. L. Luo, H. Shen, Y. Bao, H. Yin, S. Jiang, Y. Huang, S. Guo, S. Gao, D. Xing, Ze. Li, and J. Sun: *J. Magn. Magn. Mater.*, 2020, vol. 507, p. 166856.
21. D. Garzón, O. Arnache, R. Aristizabal, A. Santacruz, C. Ostos, and A. Echavarria: *J. Phys. Conf. Ser.*, 2019, vol. 1247, p. 1012012.
22. V. Chaudhary, D.V. Maheswar Repaka, A. Chaturvedi, I. Sridhar, and R.V. Ramanujan: *J. Appl. Phys.*, 2014, vol. 116, p. 163918.
23. V. Chaudhary and R.V. Ramanujan: IEEE Magn. *Lett.*, 2015, vol. 6, p. 1.
24. V. Chaudhary and S. Ramanujan: *Sci. Rep.*, 2016, vol. 6, p. 35156. https://doi.org/10.1038/srep35156.
25. E.C. Passamani, J.R.B. Tagarro, E. Nunes, and A.Y. Takeuchi: *J. Magn. Magn. Mater.*, 2002, vol. 247, pp. 191–199.
26. N.V. Mushnikov, A.G. Popov, V.S. Gaviko, A.V. Protasov, N.M. Kleinerman, O.A. Golovnya, and S.P. Naumov: *Acta Mater.*, 2022, vol. 240, p. 18330.
27. F. Maccari, D.Y. Karpenkov, E. Semenova, A.Y. Karpenkov, I.A. Radulov, K.P. Skokov, and O. Gutfleisch: *J. Alloys Compd.*, 2020, vol. 836, pp. 155338.
28. Y.A. Abdu, T. Ericsson, and H. Annersten: *J. Magn. Magn. Mater.*, 2004, vol. 280, pp. 395–403.
29. D. Garzón, J.E. Diosa, C. Ostos, F.H. Sánchez, G.A. Muñoz Medina, F. Sieves, and O. Arnache: *Mater Charact*, 2021, vol. 179, p. 111329.
30. D.G. Rancourt and J.Y. Ping: *Nucl. Instrum. Methods Phys. Res. Sect. B.*, 1991, vol. 58, pp. 85–97.
31. C. Chang, B. Shen, and A. Inoue: *Appl. Phys. Lett.*, 2006, vol. 89, 051912.
32. V. Chaudhary and R. Ramanujan: *J. Phys. D Appl. Phys.*, 2015, vol. 48, p. 305003.
33. L.M. Moreno-Ramírez, C. Romero-Muñiz, J.Y. Law, V. Franco, A. Conde, I.A. Radulov, F. Maccari, K.P. Skokov, and O. Gutfleisch: *Acta Mater.*, 2018, vol. 160, pp. 137–146.
34. J. Eckert, J.C. Holzer, and W.L. Johnson: *J. Appl. Phys.*, 1993, vol. 73, pp. 131–141.
35. V.G. Harris, K.M. Kemner, B.N. Das, N.C. Koon, A.E. Ehrlich, J.P. Kirkland, J.C. Woicik, P. Crespo, A. Hernando, and A. Garcia Escorial: *Phys. Rev. B*, 1996, vol. 54, pp. 6929–6940.
36. A. Guittoum, A. Layadi, A. Bourzami, H. Tafat, N. Souami, S. Boutarfaia, and D. Lacour: *J. Magn. Magn. Mater.*, 2008, vol. 320, pp. 1385–1392.
37. A.F. Lehlooh and S.H. Mahmood: *Hyperfine Interact.*, 2002, vol. 139, pp. 387–392.
38. J.W. Kondoro and S.J. Campbell: *Hyperfine Interact.*, 1990, vol. 55, pp. 993–999. https://doi.org/10.1007/BF02397112.
39. B. Arcondo, J. Moya, F. Audebert, and H. Sirkin: *Hyperfine Interact.*, 1994, vol. 94, pp. 2157–2161. https://doi.org/10.1007/BF02063755.
40. L.J. Swartzendruber, V.P. Itkin, and C.B. Alcock: *J. Phase Equilib.*, 1991, vol. 12, pp. 288–312.
41. C.W. Yang, D.B. Williams, and J.I. Goldstein: *J. Phase Equilib.*, 1996, vol. 17, pp. 522–531.
42. M. Khitouni, N. Njah, and D. Gilbon: *Scr. Mater.*, 2004, vol. 50, pp. 77–81.
43. J. Zamora, I. Betancourt, and J.A. García Hinojosa: *Metals.*, 2022, vol. 12, p. 994.
44. P. Allia, M. Baricco, P. Tiberto, and F. Vinai: *Phys. Rev. B*, 1993, vol. 47, pp. 3118–3125.
45. P. Allia, M. Barricco, M. Knobel, P. Tiberto, and F. Vinai: *J. Magn. Magn. Mater.*, 1994, vol. 133, pp. 243–247.
46. A. Arrott and J.E. Noakes: *Phys. Rev. Lett.*, 1967, vol. 19, pp. 786–789.
47. D.V. Maheswar, V. Sharma, and R.V. Ramanujan: *J. Alloys Compd.*, 2017, vol. 690, pp. 575–582.
48. R. Wu, F. Shen, F. Hu, J. Wang, L. Bao, L. Zhang, Y. Liu, Y. Zhao, F. Liang, W. Zuo, J. Sun, and B. Shen: *Sci. Rep.*, 2016, vol. 6, p. 20993.
49. B.K. Banerjee: *Phys. Lett.*, 1964, vol. 12, pp. 16–17.
50. A. Conde, I. Radulov, K.P. Skokov, and O. Gutfleisch: *Nat. Commun.*, 2018, vol. 9, p. 2680.
51. V. Sharma, D.V.M. Repaka, V. Chaudhary, and R.V. Ramanujan: *J. Phys. D Appl. Phys.*, 2017, vol. 50, p. 145001.
52. M.E. Fisher, S. Ma, and B.G. Nickel: *Phys. Rev. Lett.*, 1972, vol. 29, p. 917.
53. V. Chaudhary and R.V. Ramanujan: *IEEE Magn. Lett.*, 2015, vol. 6, pp. 1–4.
54. P. Nisha, S. Savitha Pillai, M.R. Varma, and K.G. Suresh: *Solid State Sci.*, 2012, vol. 14, pp. 40–47.
55. L. Zhang, M. Hui Han, H. Ge, C.J. Du, W. Wei, J. Fan, C. Zhang, L. Pi, and Y. Zhang: *Sci. Rep.*, 2016, vol. 6, p. 22397.
56. V. Singh, P. Bag, R. Rawat, N. Ramesh: *Sci. Rep.*, 2020, vol. 10.
57. V. Franco, J.S. Blázquez, and A. Conde: *Appl. Phys. Lett.*, 2006, vol. 89, p. 222512.
58. H. Yin, J. Law, Y. Huang, V. Franco, S.J. Hongxian, Y. Bao, and J. Sun: *Mater. Des.*, 2021, vol. 206, p. 109824.
59. J.Y. Law and V. Franco: *J. Mater. Res.*, 2023, vol. 38(1), pp. 37–51.
60. P. Konieczny, D. Czernia, and T. Kajiwara: *Sci. Rep.*, 2022, vol. 12, p. 16601.